Monthly Notices
of the
ROYAL ASTRONOMICAL SOCIETY

MNRAS **481,** 2371–2383 (2018)
Advance Access publication 2018 September 4

doi:10.1093/mnras/sty2405

Low redshift baryon acoustic oscillation measurement from the reconstructed 6-degree field galaxy survey

Paul Carter [1]★ Florian Beutler [1,2] Will J. Percival,[3,4,1] Chris Blake,[5,6] Jun Koda[6,7,8] and Ashley J. Ross [9]

[1]*Institute of Cosmology & Gravitation, University of Portsmouth, Dennis Sciama Building, Portsmouth PO1 3FX, UK*
[2]*Lawrence Berkeley National Lab, 1 Cyclotron Rd, Berkeley, CA 94720, USA*
[3]*Department of Physics and Astronomy, University of Waterloo, 200 University Ave W, Waterloo, ON N2L 3G1, Canada*
[4]*Perimeter Institute for Theoretical Physics, 31 Caroline St. North, Waterloo, ON N2L 2Y5, Canada*
[5]*Centre for Astrophysics & Supercomputing, Swinburne University of Technology, PO Box 218, Hawthorn, VIC 3122, Australia*
[6]*ARC Centre of Excellence for All-sky Astrophysics (CAASTRO), VIC 3010, Australia*
[7]*INFN Sezione di Roma 3, Via della Vasca Navale 84, Rome I-00146, Italy*
[8]*Dipartimento di Matematica e Fisica, Universitá degli Studi Roma Tre, via della Vasca, Navale 84, I-00146 Roma, Italy*
[9]*Center for Cosmology and AstroParticle Physics, The Ohio State University, Columbus, OH 43210, USA*

Accepted 2018 August 24. Received 2018 August 24; in original form 2018 March 5

ABSTRACT

Low-redshift measurements of baryon acoustic oscillations (BAO) measure the late-time evolution of the Universe and are a vital probe of dark energy. Over the past decade both the 6-degree Field Galaxy Survey (6dFGS) and Sloan Digital Sky Survey Main Galaxy Sample (SDSS MGS) have provided important distance constraints at $z < 0.3$. In this paper we re-evaluate the cosmological information from the BAO detection in 6dFGS making use of halo occupation distribution (HOD)-populated COmoving Lagrangian Acceleration (COLA) mocks for an accurate covariance matrix and take advantage of the now commonly implemented technique of density field reconstruction. For the 6dFGS data, we find consistency with the previous analysis, and obtain an isotropic volume-averaged distance measurement of $D_V(z_{\rm eff} = 0.097) = \left[372 \pm 17(\pm^{98}_{33})\right] (r_s/r_s^{\rm fid})\,{\rm Mpc}$ but with a highly non-Gaussian likelihood. We combine our measurement from both the post-reconstruction clustering of 6dFGS and SDSS MGS offering an updated constraint in this redshift regime, $D_V(z_{\rm eff} = 0.122) = \left[539 \pm 17(\pm^{35}_{39})\right] (r_s/r_s^{\rm fid})\,{\rm Mpc}$. This measurement tightens the constraint in comparison to the result from SDSS MGS alone, especially at the 2σ and higher significance levels. These measurements are consistent with standard Λcold dark matter (ΛCDM) and after fixing the standard ruler using a Planck prior on $\Omega_m h^2$, the joint analysis gives $H_0 = 64.0 \pm 3.5\,{\rm km\,s^{-1}\,Mpc^{-1}}$. This result is consistent with other BAO and Cosmic microwave background (CMB) studies but is in $>2\sigma$ tension with supernova distance ladder measurements. In the near future both the Taipan Galaxy Survey and the Dark Energy Spectroscopic Instrument (DESI) will improve this measurement to 1% at low redshift.

Key words: cosmology: observations – dark energy – distance scale – large-scale structure of Universe.

1 INTRODUCTION

Utilization of the baryon acoustic peak feature, measured in the two-point statistics of redshift surveys, has enabled high-precision cosmological constraints. Within the framework of the concordance Λcold dark matter (ΛCDM) model the initial perturbations in all species were seeded following an early inflationary epoch. Following this the Universe existed in a plasma state, in which radiation and baryonic matter are strongly coupled through the process of Thomson scattering and through Coulomb forces.

Interplay between gravitational attraction and radiation pressure introduces acoustic oscillations in the primordial photon-baryon fluid. At $z \approx 1100$, the background temperature of the Universe becomes comparable to the ionization energy of electrons and recombination occurs. The mean free path of photons becomes greater than

★ E-mail: paul.carter1@port.ac.uk

the Hubble distance and they decouple from baryons at $z \sim 1020$. This process leaves the baryonic matter distributed in overdensities in a surrounding spherical shell. These shells have a co-moving radius which corresponds to the sound horizon, $r_s \sim 150$ Mpc, at the baryon drag epoch. Through mutual gravitational interaction the dark matter component grows with the baryonic component to emulate this feature (Eisenstein, Seo & White 2007a). Galaxies form in regions of overdensity and are biased tracers of the underlying total matter field on large scales.

Making use of the two-point correlation function ξ it is possible to see the effect of BAO as a peak, characterized by separation r_s. Alternatively the power spectrum gives similar information in Fourier space, with the signal translating to oscillations in amplitude with wavenumber. Measurements of the apparent scale of the BAO feature offer a robust standard ruler of the distance to the measured galaxy population's effective redshift. Measurements of this feature at different redshifts allow for a test of the general cosmological model, especially inference regarding the equation of state of dark energy (Weinberg et al. 2013).

The BAO peak is a well-studied probe of cosmology, with the first observations in the Sloan Digital Sky Survey (SDSS; York et al. 2000; Eisenstein et al. 2005) and 2-degree field (2dFGRS; Colless et al. 2001; Percival et al. 2001; Cole et al. 2005) galaxy redshift surveys. Subsequently the BAO peak has been detected in later SDSS data releases (Kazin et al. 2010; Percival et al. 2010), 6dFGS (Beutler et al. 2011), WiggleZ (Blake et al. 2011), BOSS (LOWZ and CMASS; Alam et al. 2017), eBOSS luminous red galaxies (LRGs) (Bautista et al. 2017) and quasars (QSOs; Ata et al. 2018), and a higher redshift detection using Ly α forest measurements in BOSS (Slosar et al. 2013; Font-Ribera et al. 2014; Delubac et al. 2015). The BAO has also been detected in the higher order statistics of the three-point correlation function (Slepian et al. 2017) and bispectrum (Pearson & Samushia 2017) for the BOSS CMASS DR12. The BAO feature has also been measured using voids as the clustering tracer (Kitaura et al. 2016; Liang et al. 2016) in the BOSS DR11 catalogue. These measurements have constructed a distance ladder that spans from $z = 0$ out to $z \sim 0.8$ using conventional galaxy redshift surveys, $z \sim 1.5$ through eBOSS QSOs and to $z \sim 2.3$ when including Ly α.

In recent analyses of the BAO peak, a method of density field reconstruction has been employed. Eisenstein et al. (2007b) proposed that, as the bulk flows that smear the acoustic peak are sourced from the density field potential itself, the galaxy map can itself be used to estimate the displacement field. Removal of these shifts has been shown to reduce the damping of the BAO and increase the signal to noise (S/N) of this feature. This increased S/N results from higher order statistics which have been moved back into linear fluctuations (Schmittfull et al. 2015; Slepian et al. 2017).

Density field reconstruction has been applied in recent work on surveys including SDSS (Padmanabhan et al. 2012; Ross et al. 2015), WiggleZ (Kazin et al. 2014), and throughout BOSS (Alam et al. 2017). These studies use either a perturbation-theory-based approach that relies on the finite difference method (Noh, White & Padmanabhan 2009; Padmanabhan, White & Cohn 2009), or an alternative FFT-based iterative algorithm (Burden et al. 2014; Burden, Percival & Howlett 2015).

This paper explores the application of density field reconstruction to 6dFGS following from the initial detection of the BAO peak by Beutler et al. (2011). Aside from providing post-reconstruction constraints, the paper also improves on the analysis of errors, using high fidelity COmoving Lagrangian Acceleration (COLA)-based mock catalogues (Tassev, Zaldarriaga & Eisenstein 2013; Howlett, Manera & Percival 2015; Koda et al. 2016) to provide more accurate covariance matrices than the lognormal approach adopted previously. We also combine with the Ross et al. (2015) lowest redshift measurement using the SDSS-II Main Galaxy Sample (MGS). This combined low-redshift measurement is useful in further constraining H_0 for cosmological tests of dark energy. Also this offers an independent test of the Hubble parameter in the similar low-redshift regime as supernovae surveys (Riess et al. 2016). There is currently ongoing tension between distance ladder measurements and those from BAO and Cosmic Microwave Background (CMB) studies (Planck Collaboration et al. 2015; Di Valentino, Melchiorri & Silk 2016; Riess et al. 2016)

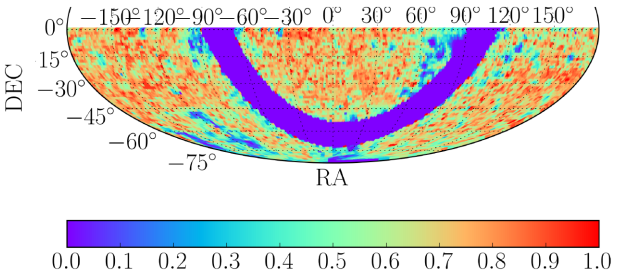

Figure 1. The sky coverage of the 6dFGS *K*-band sample, the colour of each cell corresponds to the completeness in that region. This total completeness constitutes a combination of sky and magnitude completeness of galaxies.

This paper is organized as follows: Section 2 offers an overview of the final 6dFGS data set and describes the catalogue used in this study. Section 3 outlines the use of halo occupation distribution (HOD) modelling to develop high-fidelity COLA-based mock catalogues. Section 4 gives a summary of the clustering statistic measurement made during this work and the formalism for density field reconstruction. Section 5 provides the BAO fitting model and constraints extracted both before and after reconstruction. Following this a number of tests regarding the mock population and robustness of results are conducted in Section 6. Section 7 provides a joint analysis with SDSS DR7 MGS data and the cosmological interpretation of these results. Finally, our conclusions are given in Section 8.

Our analysis uses a fiducial flat ΛCDM model cosmology, which is close to Planck 2015 (Planck Collaboration et al. 2015), with parameters $\Omega_m^{\rm fid} = 0.31$, $\Omega_\Lambda^{\rm fid} = 0.69$, $h = 0.6777 = H_0/[100\,{\rm km\ s^{-1}\ Mpc^{-1}}]$, and the fiducial sound horizon size at the drag epoch is $r_s(z_d) = 147.5$ Mpc.

2 THE 6DF GALAXY SURVEY

The 6dF Galaxy Survey[1] (6dFGS; Jones et al. 2009) combines peculiar velocities and redshifts for galaxies covering almost the entire Southern hemisphere. The survey was conducted between 2001 and 2006 using the 6-degree Field multifibre instrument on the UK Schmidt Telescope and covers 17 000 deg^2 of the sky with a median redshift 0.053. The sample selected for this work is the same as that used in Beutler et al. (2011), selected with a magnitude cut of $K < 12.9$ and imposing a cut for regions with $< 60\%$ completeness (Jones et al. 2006). This gives a catalogue of 75 117 galaxies. In Fig. 1 the sky coverage and total completeness distribution of galaxies in this final catalogue are presented. Further details

[1]The data, randoms, and mock catalogues used during this work are available at: http://www.6dfgs.net/downloads/6dFGS_Recon_Files.tar.gz

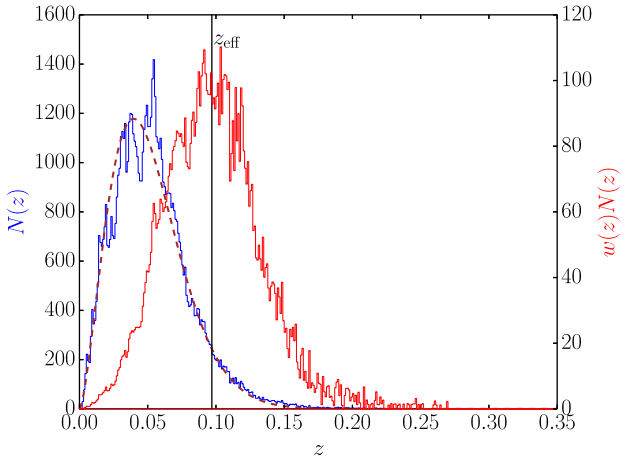

Figure 2. The unweighted (blue) and FKP weighted (red) redshift distribution of 6dFGS, with the best-fitting model (brown dashed line) of $N_{\rm fit}(z)$ to the unweighted distribution. This spline fit to the unweighted distribution is used in the FKP weights. The effective redshift of the 6dFGS in given as the black vertical line.

regarding the structure and systematics in the full 6dFGS can be found in Jones et al. (2009).

Throughout this work galaxies have S/N (FKP) weights applied (Feldman, Kaiser & Peacock 1994). These weights $w_{\rm FKP}(z) = 1/(1 + n(z)P_0)$, optimize the S/N between sample variance and shot noise at a particular fiducial wavenumber, where P_0 is the amplitude of the power spectrum at this wavenumber and $n(z)$ is the number density. 6dFGS has a high density gradient with redshift, and therefore this weighting scheme has a strong impact on the analysis. We chose to use $P_0 \sim 10\,000\,{\rm h}^{-3}$ Mpc^3 approximately the amplitude where the BAO signal peaks, $k_{\rm eff} \sim 0.15\,{\rm h}$ Mpc^{-1} (Seo & Eisenstein 2007). A fit to the unweighted redshift distribution is used to calculate $n(z)$ for the weighting. The form of this model is $N_{\rm fit}(z) = Az^{\gamma}\exp[-(z/z_p)^{\gamma}]$ with the best-fitting parameters $A = 456$, 500, $z_p = 0.03967$, and $\gamma = 1.5369$ (Jones et al. 2009). The redshift distributions, both unweighted and once the FKP weighting scheme has been applied, are shown in Fig. 2. The effective redshift of the total weighted sample is $z_{\rm eff} = 0.097$ defined via

$$z_{\rm eff} = \frac{\sum_{i=0}^{N_g} z_i\, w_i(z)}{\sum_{i=0}^{N_g} w_i(z)}. \quad (1)$$

3 COLA-BASED MOCK CATALOGUES

Mock catalogues are produced based on numerical simulations and populated using a HOD model. We construct our covariance matrix from 600 of these realizations that simulate the survey volume.

3.1 COLA simulations

In an ideal world the underlying dark matter haloes would be generated using *N*-body simulations in order to fully encapsulate the non-linear regime; this is computationally expensive. Instead we make use of the COLA method (Tassev et al. 2013; Howlett et al. 2015; Koda et al. 2016) to produce our 6dFGS mock catalogues.

The COLA method allows for an increase in efficiency by combining *N*-body simulations with 2nd-order Lagrangian Perturbation Theory (2LPT). By allowing 2LPT to solve the large-scale distribution exactly and only using time-stepping for the small scales, COLA outperforms classical *N*-body simulations in computational speed by orders of magnitude.

To run the COLA simulations we used 432 cores and 8 GB of memory per core on the Raijin supercomputer at the Australian National Computational Infrastructure (NCI), with each run taking ∼45 min on Intel Xeon Sandy Bridge 2.6 GHz, and Broadwell 2.6 GHz processing cores. The mocks produced consist of $(1728)^3$ particles in boxes of each $1.2\,{\rm h}^{-1}$ Gpc on a side. COLA takes 20 time-steps from initialization down to $z = 0$ in our runs. The mass resolution of the mock catalogues is $2.8 \times 10^{10}\,{\rm h}^{-1}{\rm M}_{\odot}$ and a friends-of-friends (FoF) finder is used to locate haloes that consist of a minimum of 32 dark matter particles. This mass resolution of haloes is satisfied by our $M_{\rm min}$ HOD parameter at $z > 0.045$ and hence galaxies at redshift above this are almost all fully resolved. The initial fiducial cosmology used in these mocks is $\Omega_m = 0.3$, $\Omega_b = 0.0478$, $h = 0.68$, $\sigma_8 = 0.82$, and $n_{\rm s} = 0.96$. To ensure our simulation matches the data catalogue, snapshots at $z = 0.1$ were used to build the mock surveys, close to the effective redshift of the data.

The fundamental mass resolution of the mock catalogue does mean that we are not able to replicate the low-mass haloes observed at low redshift. This will lead to a discrepancy between data and mock at $z < 0.05$ in the HOD population. This does not impact the BAO analysis on large scales; the reduction of number density at low redshift from a lack of these low-mass galaxies only contributes to a reduction in effective volume of 1.0%, which is the main component of the error-bars. Potential second-order effects on the errors through undersampling of low-redshift galaxies would be sub-leading and only enter our model fit through the covariance matrix.

3.2 Halo occupation distribution model

As is common in HOD modelling, we separate the clustering contributions of massive central and satellite galaxies. The mean occupation function for a dark matter halo of mass M hosting each type is respectively (Zheng et al. 2005)

$$\langle N_{\rm C}(M)\rangle = \frac{1}{2}\left[1 + {\rm erf}\left(\frac{\log_{10} M - \log_{10} M_{\rm min}}{\sigma_{\log M}}\right)\right], \quad (2)$$

and

$$\langle N_{\rm S}(M)\rangle = \left(\frac{M - M_{\rm min}}{M_1}\right)^{\alpha}, \quad (3)$$

in which $M_{\rm min}$ is the minimum dark matter halo mass that can host a central galaxy, M_1 is the mass of a halo that on average contains one additional satellite member, and $\sigma_{\log M}$ (Zehavi et al. 2011) allows for a gradual transition from $\langle N_{\rm C}(M)\rangle = 0$ to $\langle N_{\rm C}(M)\rangle = 1$. When assigning the satellites to the halo, their peculiar velocities are randomly selected based on the virial velocity of the halo assuming a spherical Navarro, Frenk & White (1996) profile. The total halo occupation is the sum of the mean central and mean satellite per central because a dark matter halo can only host a satellite if it already has a central galaxy;

$$\langle N_t(M)\rangle = \langle N_C(M)\rangle\,(1 + \langle N_S(M)\rangle)\,. \quad (4)$$

The halo model (Ma & Fry 2000; Peacock & Smith 2000; Seljak 2000; Cooray & Sheth 2002) accounts separately for clustering between galaxies in the same halo (1-halo term $\xi_{1h}(r)$) and those in different haloes (2-halo term $\xi_{2h}(r)$), which contribute to the correlation function on small scales and large scales, respectively.

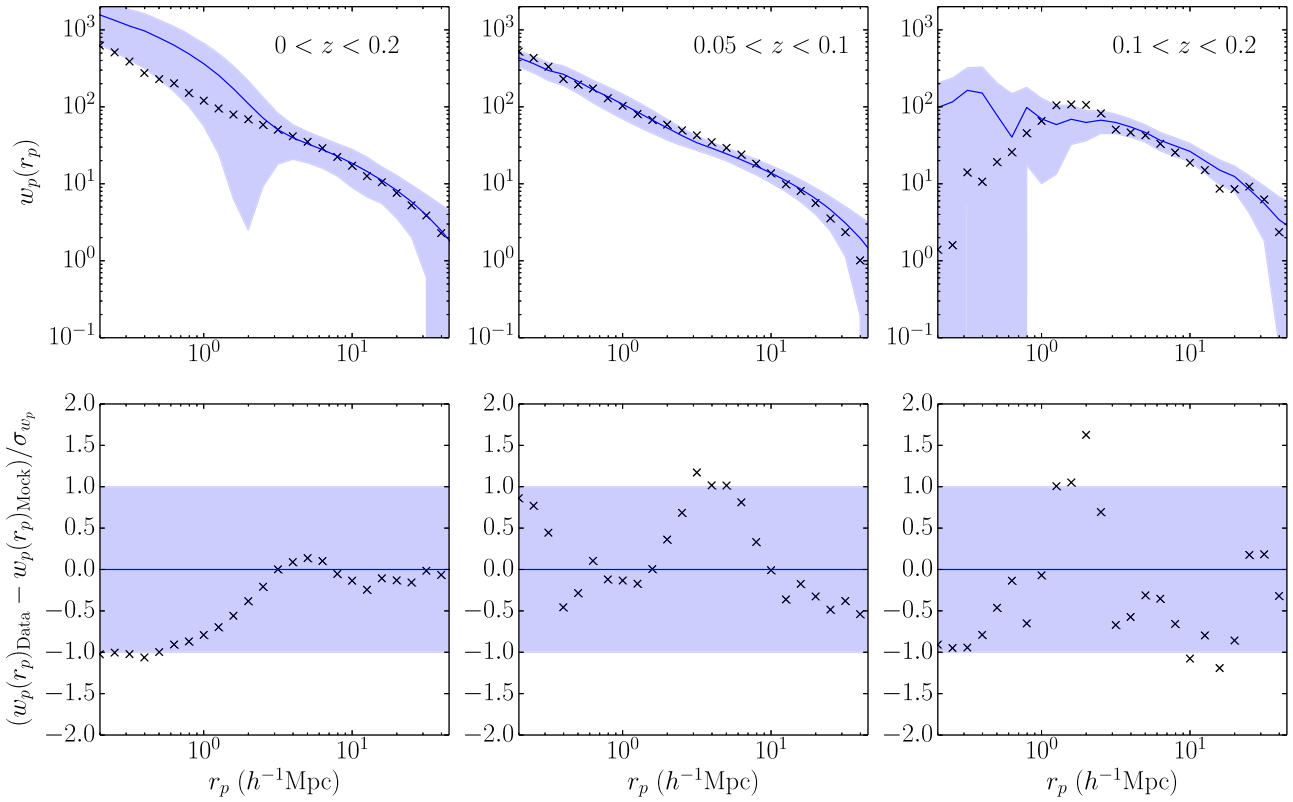

Figure 3. Comparison between the projected correlation function of the data and the mean of the mock catalogues where the blue line shows the COLA mock and the black points the data. The upper second and third plots show a split of the full redshift range in the first panel into two sub-intervals. The lower panels show the difference normalized by the standard deviation. There is good agreement at $z > 0.05$; the mocks show a larger amplitude in the clustering in the 1-halo component because of the low mass resolution. The blue shaded regions correspond to 1σ error; deviations outside of this are accounted for within statistical fluctuation and by the fact that there are correlations between neighbouring bins.

The total correlation function is just the superposition of these terms $\xi(r) = \xi_{1h}(r) + \xi_{2h}(r)$.

3.2.1 *Fitting of the HOD model*

To replicate the data, both the redshift distribution $n(z)$ and projected correlation function $w_{\rm p}(r_{\rm p})$

$$w_{\rm p}(r_{\rm p}) = 2\int_0^{\pi_{\rm max}} {\rm d}\pi\, \xi(r_{\rm p}, \pi) \tag{5}$$

are used to measure the HOD parameters. $r_{\rm p}$ and π correspond to the separation between galaxies perpendicular and parallel to the line of sight, respectively. When integrating along the line of sight we use $\pi_{\rm max} = 50{\rm h}^{-1}$ Mpc, producing a statistic that has negligible contribution from the Fingers-of-God (FoG) redshift space distortion (RSD) effect (Hamilton 1998).

The redshift dependence of the HOD model is parametrized through a polynomial in $M_{\rm min}$,

$$\log_{10}(M_{\rm min}(z)) = a + bx + cx^2 + dx^3 + fx^4, \tag{6}$$

where $x = z - 0.05$. The ratio of $\log_{10}(M_1/M_{\rm min})$ is approximately constant in redshift (used as a free parameter in our HOD fit) and hence $\log_{10}(M_1(z))$ adopts a redshift dependence in order to achieve this. The order of the polynomial fit was set by the order at which the relative error on $n(z)$ did not change (from 3rd to 4th order). We generate mocks for a grid of HOD parameters ($\log_{10}(M_1/M_{\rm min})$, $\sigma_{\log M}$, α) and measure the projected correlation function and number density to fit against the data. We find the best-fitting HOD parameters of $\alpha = 1.50 \pm 0.05$, $\sigma_{\log M} = 0.50 \pm 0.12$, and $\log_{10}(M_1/M_{\rm min}) = 1.50 \pm 0.08$ where the polynomial terms are $a = 12.0448$, $b = 22.8194$, $c = 110.4364$, $d = -1435.6529$, and $f = 3679.3770$.

The match in projected correlation function and redshift distribution between the best-fitting mock and the data are shown in Figs 3 and 4. The mocks are a good fit at $z > 0.05$, but at a lower redshift this breaks down due to the small scale mass resolution issue in the COLA simulation. As mentioned earlier this discrepancy does not contribute to the analysis on large scales and the reduction of number density at low redshift only contributes to a reduction in effective volume of 1%.

We assign a central galaxy to a halo according to the mean occupation $\langle N_{\rm C}(M)\rangle$, and draw a random number of satellites from a Poisson distribution with mean $\langle N_{\rm S}(M)\rangle$ if the halo hosts the central galaxy. The position and the velocity of the central galaxies are those of the mean of the halo particles (center of mass). We note that this is an assumption made for the central galaxies and there is some observational evidence that these galaxies have a slight non-halo-centric position and relative velocity (Guo et al. 2015, 2016). Satellite galaxies have distances from the halo centre randomly sampled from an isotropic NFW profile (Navarro et al. 1996) with a concentration parameter (Bullock et al. 2001). We assign a Gaussian random velocity based on the radius-dependent velocity-dispersion profile in addition to the halo velocity (van den Bosch et al. 2004; de la Torre et al. 2013).

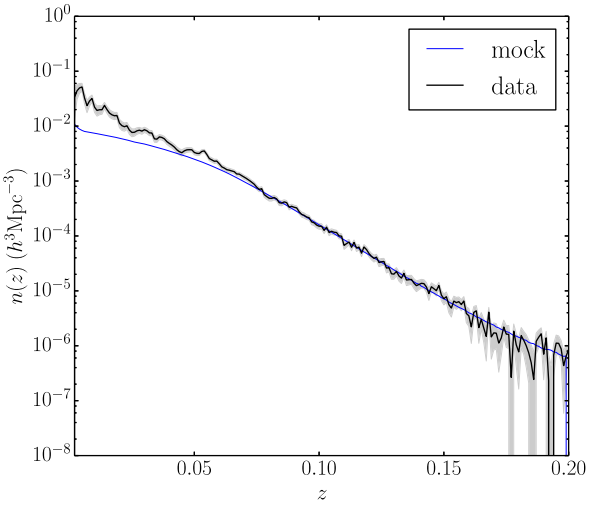

Figure 4. The redshift distribution of the data and the mean of the mock catalogues. The mock and data are consistent in the redshift range $z > 0.05$, while at $z < 0.05$ the mock shows a lower density due to the resolution limit of the COLA mocks.

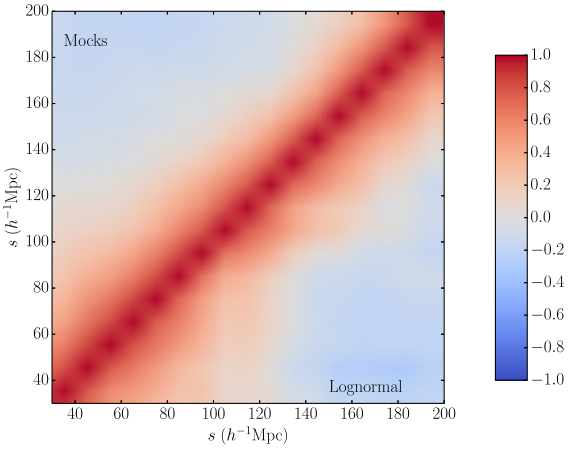

Figure 5. Comparison of the COLA mock and lognormal based correlation matrices. The correlation in the mock covariance matrix has been reduced in comparison to the lognormal based matrix.

4 OVERVIEW OF CLUSTERING MEASUREMENT

In this section, we explain how we measure the correlation function and its covariance matrix. We will also introduce density field reconstruction, which we apply to the data set.

4.1 Two-point correlation function

We measure the two-point correlation statistic using the Landy & Szalay (1993) estimator

$$\xi(s) = 1 + \frac{\mathrm{DD(s)}}{\mathrm{RR(s)}}\left(\frac{n_\mathrm{r}}{n_\mathrm{d}}\right)^2 - 2\frac{\mathrm{DR(s)}}{\mathrm{RR(s)}}\left(\frac{n_\mathrm{r}}{n_\mathrm{d}}\right), \tag{7}$$

where DD(s), DR(s), and RR(s) are the pair counts of data–data, data–random and random–random pairs in different co-moving redshift space separation bins, s. The random catalogues used during this analysis were generated using the selection function measured from the data catalogue. This Monte Carlo samples the sky coverage (as given in Fig. 1) and redshift distribution using 30 times as many random points as galaxies, to ensure that the Poisson noise contribution from the randoms is significantly smaller than that from the galaxies. This number of randoms was verified to be sufficient as when reduced to 25 times there was no change to the results. The normalization of pair counts is performed with n_d and n_r which are the weighted number of objects for data and random catalogues, respectively.

The data–data pair counts have been assigned a fibre collision weight for each galaxy pair. The design of the 6dF instrument only allowed fibres to be placed greater than 5.7 arcmin apart resulting in lost pairs at small angular separations. By allowing for multiple passes in the targeting plan, this effect of lost pairs is minimized for 70% of the survey area. The remaining 30% requires an upweighting of pair counts to ensure we do not bias the clustering statistics. This angular weight $w_f(\theta_{12})$ is calculated as a ratio between the target angular correlation function created from the photometric survey used to target the spectroscopy, and the observed angular correlation function (Hawkins et al. 2003; Jones et al. 2004; Beutler et al. 2013); θ_{12} is the angle between galaxies in the pair. This approximation works when radial clustering is matched between observed and unobserved pairs. On small scales this is not true and we should instead use a scheme such as that of Bianchi & Percival (2017). As we are only interested in the BAO scale, this is not necessary for this analysis.

4.2 Covariance matrix

A covariance matrix was generated from 600 mock realizations, built on COLA-based simulations and populated through a HOD parametrization as described in Section 3.

The covariance matrix is given by

$$\boldsymbol{C}_{ij} = \frac{1}{N-1}\sum_{n=1}^{N}\left[\xi_n(s_i) - \overline{\xi}(s_i)\right]\left[\xi_n(s_j) - \overline{\xi}(s_j)\right], \tag{8}$$

in which the summation runs over N-mock realizations. $\xi_n(s_i)$ is the ith separation bin of the nth mock correlation function and $\overline{\xi}(s_i)$ is the average in the ith bin. The uncertainties on the correlation functions shown in Figs 6–8 are from the standard deviation on the diagonal $\sqrt{\boldsymbol{C}_{ii}}$, while during the fitting of models the full covariance matrix is used.

The correlation matrix (defined $R_{ij} = C_{ij}/\left[\sqrt{C_{ii}}\sqrt{C_{jj}}\right]$) without reconstruction is compared to that previously used based on lognormal catalogues (Beutler et al. 2011) in Fig. 5. This comparison shows that the correlation between neighbouring bins has decreased using the COLA mocks. The correlation functions of the mock catalogues are compared to that from the data in Fig. 6 showing good agreement. These mock catalogues have been used in other recent work on the 6dFGS (Achitouv et al. 2017; Blake, Carter & Koda 2018).

4.3 FFT-based density field reconstruction

The formalism used for density field reconstruction follows from Burden et al. (2014, 2015). In a Lagrangian framework the Eulerian position of a particle is given by

$$\mathrm{x}(\mathrm{q}, t) = \mathrm{q} + \boldsymbol{\Psi}(\mathrm{q}, t), \tag{9}$$

where $\mathbf{q}$ is the Lagrangian position, x is the Eulerian position, and $\boldsymbol{\Psi}$ is the displacement vector field. Implementing first order Lagrangian Perturbation Theory (LPT) the standard Zel'dovich ap-

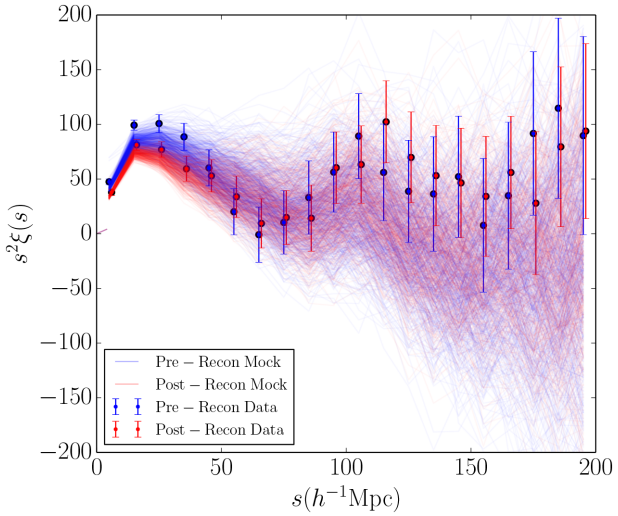

Figure 6. The distribution of all 600 mock correlation functions, both pre- (blue) and post-reconstruction (red). The data points show the 6dFGS correlation function with errors from the diagonal of the constructed COLA mock covariance matrix. The post-reconstruction data points have been displaced by $+1\,h^{-1}$ Mpc for clarity. Retrieval of the real-space post-reconstruction density field results in a reduction of the amplitude in the correlation function.

proximation (Zel'dovich 1970) can be obtained

$$\boldsymbol{\Psi}_{(1)}(\mathrm{k}) = -\frac{i\mathrm{k}}{k^2}\delta_{(1)}(\mathrm{k}), \tag{10}$$

which relates the Fourier transform of the first-order overdensity field $\delta_{(1)}$ to the displacement field in **k**-space. To linear order galaxies trace the matter density field as $\delta_\mathrm{g} = \mathrm{b}\delta_\mathrm{m}$, where b is the bias. Because of the redshift space distortions (RSD), to obtain the displacement field Ψ, we actually have to solve the differential equation

$$\nabla\cdot\boldsymbol{\Psi} + \frac{f}{\mathrm{b}}\nabla\cdot(\boldsymbol{\Psi}\cdot\hat{\boldsymbol{r}})\hat{\boldsymbol{r}} = -\frac{\delta_g}{\mathrm{b}}. \tag{11}$$

On linear scales RSD enhance the clustering along the line of sight, dependent on the amplitude of $f = d\ln D(a)/d\ln a$ the logarithmic derivative of the growth rate, $D(a)$ the linear growth rate, a the scale factor, and σ_8 is the rms amplitude of the clustering averaged over spheres of $8\,h^{-1}$ Mpc. In the limit of $f \to 0$ in equation (11) we recover equation (10), which would be the case if the field were in real space.

Equation (11) can be solved as in Padmanabhan et al. (2012) using a finite difference approximation to compute the gradients. This sets up a grid in configuration space through which the potential can be described as a linear system of equations. This methodology was chosen because although $\boldsymbol{\Psi}$ is irrotational, the term $(\boldsymbol{\Psi}\cdot\hat{\boldsymbol{r}})\hat{\boldsymbol{r}}$ is not, hence a simple solution cannot be found with Fourier methods. However, Burden et al. (2015) showed that by making the approximation that $(\boldsymbol{\Psi}\cdot\hat{\boldsymbol{r}})\hat{\boldsymbol{r}}$ is irrotational and iterating after correcting, one can efficiently obtain the correct solution using FFTs (with IFFT referring to the Inverse Fast Fourier Transform)

$$\boldsymbol{\Psi} = \mathrm{IFFT}\left[-\frac{i\mathrm{k}\delta(k)}{k^2 b}\right] - \frac{f}{1+f}\left(\mathrm{IFFT}\left[-\frac{i\mathrm{k}\delta(k)}{k^2 b}\right]\cdot\hat{\mathbf{r}}\right)\hat{\mathbf{r}}. \tag{12}$$

The displacement field calculated from this form of the algorithm has been shown to agree with the finite difference approach and causes negligible differences between post-reconstruction two-point statistics (Burden et al. 2014).

To also remove RSD we modify the displacement vector as $\Psi^\mathrm{final} = \Psi + \Psi_\mathrm{RSD}$ (Kaiser 1987; Padmanabhan et al. 2012) where

$$\Psi_\mathrm{RSD} = -f(\Psi\cdot\hat{\mathbf{r}})\hat{\mathbf{r}}, \tag{13}$$

using the already calculated displacement field along the line of sight. This retrieval of the real-space post-reconstruction density field results in a reduction of the amplitude in the correlation function (Fig. 6).

5 CORRELATION FUNCTION MODELLING

In Beutler et al. (2011) a model for the pre-reconstruction correlation function was constructed from the formalism of Crocce & Scoccimarro (2008). Here we use a model that marginalizes over the shape of the correlation function through a number of nuisance parameters (Anderson et al. 2014). A physically motivated model for the post-reconstruction correlation function at $s > 30\,h^{-1}$ Mpc is not readily available and so marginalization of the broad-band shape is important to ensure we are capturing the BAO information only.

The fit of the model $\mathbf{m}(s)$ to the data $\mathbf{d}(s)$ is determined through a minimum-χ^2 fitting, $\chi^2 = \mathbf{D}^T\mathbf{C}^{-1}\mathbf{D}$, where $\mathbf{D} = \mathbf{d}(s) - \mathbf{m}(s)$. In our standard analysis we use a fitting range of $30\,h^{-1}$ Mpc $< s <$ $200\,h^{-1}$ Mpc over 17 bins. The inverse covariance matrix used was built from the set of 600 mocks correcting for statistical bias in the standard way (Hartlap, Simon & Schneider 2007).

5.1 Template formalism

The fitting of the correlation function relies primarily on a template model with damped BAO given in Eisenstein et al. (2007a). The model power spectrum that is used in this template contains a linear model $P_\mathrm{lin}(k)$ from CAMB (Lewis, Challinor & Lasenby 2000) and a no-wiggle power spectrum $P_\mathrm{nw}(k)$ (Eisenstein & Hu 1998)

$$P^\mathrm{mod}(k) = P_\mathrm{nw}(k)\left[1 + \left(\frac{P_\mathrm{lin}(k)}{P_\mathrm{nw}(k)} - 1\right)e^{-\frac{1}{2}k^2\Sigma_\mathrm{nl}^2}\right]. \tag{14}$$

The no-wiggle model has had the BAO feature removed whilst retaining the overall shape. The template $\xi^\mathrm{mod}(s)$ is then obtained from this through a Hankel transform and used with five nuisance parameters (B_ξ, a_1, a_2, a_3, and Σ_nl) which allow marginalization of the BAO damping (the scale of which is set by Σ_nl) and broad-band shape of the correlation function

$$\xi^\mathrm{fit}(s) = B^2\xi^\mathrm{mod}(\alpha s) + \frac{a_1}{s^2} + \frac{a_2}{s} + a_3. \tag{15}$$

α is defined as

$$\alpha = \frac{D_V(z_\mathrm{eff})r_s^\mathrm{fid}}{D_V^\mathrm{fid}(z_\mathrm{eff})r_s}, \tag{16}$$

and allows one to freely scale the BAO feature in our model. A best-fitting value of $\alpha < 1$ corresponds to a larger BAO scale compared to the fiducial cosmology used to construct our template and $\alpha > 1$ indicates a smaller BAO scale. D_V is the volume-averaged distance

$$D_V = \left[cz(1+z)^2 D_A^2(z)H^{-1}(z)\right]^{1/3}, \tag{17}$$

which is a weighted average of the co-moving angular diameter distance and Hubble parameter, with double weight given to the former due to the geometry of the measurement (two directions in the plane of the sky and one along the line of sight).

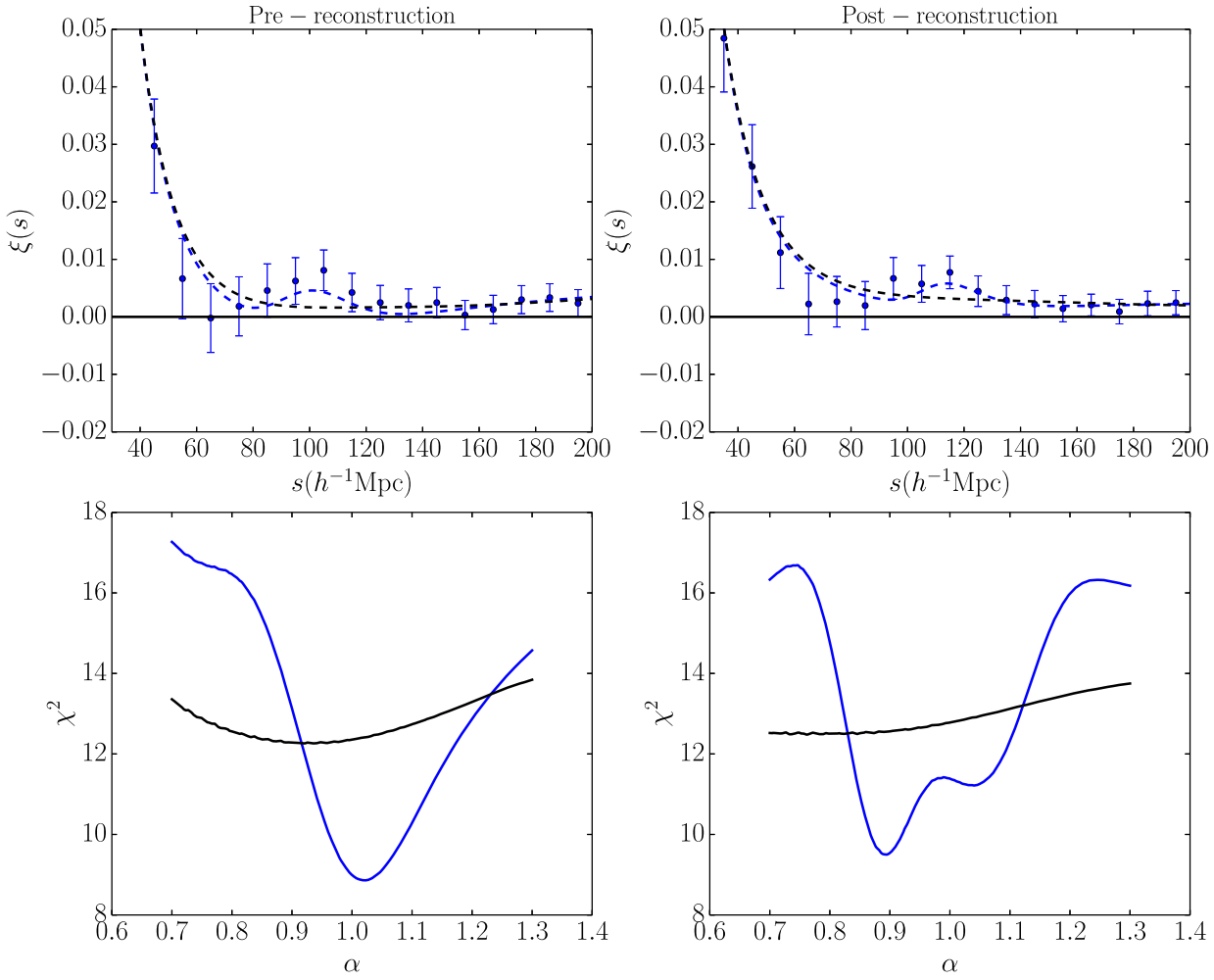

Figure 7. Left: In the upper plot the pre-reconstruction correlation function is given with the best-fitting model, corresponding to $\alpha = 1.018 \pm 0.066$. This shows consistency with the results from Beutler et al. (2011) in which they used a lognormal covariance matrix. The plot below provides the marginalized χ^2 distribution for α. Right: In the upper plot the post-reconstruction correlation function is given with the best-fitting model, corresponding to $\alpha = 0.895 \pm 0.041$. The plot below provides the marginalized χ^2 distribution for α. There is a strong bi-modality in this likelihood surface, which translates to strongly non-gaussian errors at the 2σ ($\Delta\chi^2 = 4$) level. This means that although the best fit for the 6dFGS post-reconstruction constraint was found at $\alpha < 0.9$, the likelihood also gives weight to $\alpha \sim 1.04$ when combining with MGS measurements (Section 7.2).

5.2 Pre-reconstruction

To provide constraints on the pre-reconstruction BAO peak the above template was utilized through a maximum likelihood based routine similar to that outlined in Ross et al. (2015). The model has six free parameters (B, α, a_1, a_2, a_3, and $\Sigma_{\rm nl}$) and we assume a Gaussian prior on the non-linear damping scale, $\Sigma_{\rm nl} = 10.3 \pm 2.0\,\mathrm{h^{-1}}$ Mpc as measured from the mean of the mocks (discussed in Section 6). The 1σ and 2σ uncertainties are defined at the $\Delta\chi^2 = 1$ and 4 levels, respectively, after marginalization over the nuisance parameters.

The best-fitting correlation function is compared to the data in Fig. 7. We also show the χ^2 distribution. The marginalized constraint on the shift parameter α pre-reconstruction is $\alpha = 1.018 \pm 0.067$ with χ^2/d.o.f $= 8.86/11 = 0.81$ (corresponding to a p-value of $p = 0.640$), which is consistent with Beutler et al. (2011), who used a WMAP7 fiducial cosmology and found $\alpha = 1.036 \pm 0.062$ (the α fit from our work translates to $\alpha_{\rm WMAP7} = \alpha_{\rm Planck}[(D_V^{\rm Planck}/r_s^{\rm Planck})/(D_V^{\rm WMAP7}/r_s^{\rm WMAP7})] = 1.047 \pm 0.069$ for comparison in the WMAP7 fiducial model).

5.3 Post-reconstruction

We apply density field reconstruction to both the data and COLA mock catalogues. In doing so a galaxy bias of $b = 1.82$ (Beutler et al. 2011) and a growth rate of $f(z_{\rm eff} = 0.097) = 0.579$ were assumed. Our results are independent of this choice as shown in Section 6.3, finding robustness to variations of ∼8% in these parameters. When calculating the displacement field, the overdensity field was smoothed using a Gaussian smoothing kernel, $S(k) = \exp[-(kR)^2/2]$, with a smoothing scale of $R = 15\,\mathrm{h^{-1}}$ Mpc. Using the calculated displacement field as a proxy for the non-linear evolution, the catalogues were shifted to move the field back into the pseudo-linear regime. The reconstruction algorithm gave a mean galaxy shift of $\bar{s} = 5.87\,\mathrm{h^{-1}}$ Mpc, which is around the typical

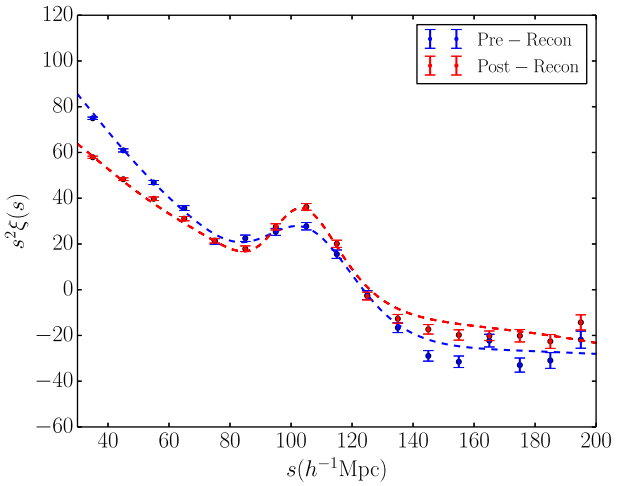

Figure 8. The best fit to the pre/post-reconstruction mean of the mock correlation functions. The improvement factor is $I \sim 1.86$ and the best-fitting non-linear damping scales are $\Sigma_{\rm nl} = 10.3\,{\rm h}^{-1}$ Mpc and $\Sigma_{\rm nl} = 4.8\,{\rm h}^{-1}$ Mpc, respectively.

displacement expected using the Zel'dovich approximation (Eisenstein et al. 2007b).

The correlation function post-reconstruction has an estimator that includes both a shifted random S and independent unshifted random catalogues R (Padmanabhan et al. 2012)

$$\xi(s) = \frac{\mathrm{SS}(s)}{\mathrm{RR}(s)}\left(\frac{n_{\rm r}}{n_{\rm s}}\right)^2 + \frac{\mathrm{DD}(s)}{\mathrm{RR}(s)}\left(\frac{n_{\rm r}}{n_{\rm d}}\right)^2 - 2\frac{\mathrm{DS(s)}}{\mathrm{RR}(s)}\left(\frac{n_{\rm r}^2}{n_{\rm d}n_{\rm s}}\right); \tag{18}$$

$n_{\rm s}$ is the weighted number of shifted objects in the random and $n_{\rm r}$ corresponds to the number in the independent unshifted catalogue.

As in the pre-reconstruction case, we use the smoothing parameter fit from the mean of the mocks with a Gaussian prior $\Sigma_{\rm nl} = 4.8 \pm 2.0\,{\rm h}^{-1}$ Mpc. The marginalized constraint on the shift parameter α post-reconstruction is $\alpha = 0.895 \pm 0.042(\pm^{0.235}_{0.079})$ with χ^2/d.o.f $= 9.49/11 = 0.86$ (the error in the bracket showing the non-Gaussianity at the 95% confidence level). The model, data, and χ^2 distribution are displayed in Fig. 7. The α post-reconstruction found has a non-Gaussian likelihood beyond the 1σ region which means that although the value is displaced from the average, it is still consistent with the mock catalogues (discussed further in Section 6).

6 TESTS ON THE MOCK CATALOGUES

6.1 Fitting the mean of the mocks

We fit both the pre/post reconstruction average correlation functions from the mock population. This fit makes use of the covariance matrices, which have been rescaled by the number of realizations N, $\mathbf{C}_{\rm mean} = \mathbf{C}_{\rm one}/N$. The best-fitting model is shown in Fig. 8 with $\alpha_{\rm pre} = 0.999 \pm 0.0065$ and $\alpha_{\rm post} = 0.997 \pm 0.0035$ giving an improvement factor of $I = \sigma_{\alpha,\,\rm pre}/\sigma_{\alpha,\,\rm post} \sim 1.86$.

6.2 Comparison between data and fits to individual mocks

To make comparisons between the mock population and the data, each of the 600 realizations used to produce the covariance matrices were individually fit. To ensure that this comparison was performed only on the mocks that have a relevant detection of the BAO feature, we select a sub-sample having 1σ contours ($\Delta\chi^2 = 1$) within the prior region $0.7 < \alpha < 1.3$ (both pre- and post-reconstruction). This cut reduces the population to 70% of its original number, a similar fraction to that found during the SDSS MGS analysis (Ross et al. 2015). Comparisons of the distributions of best-fitting χ^2, the value of α pre/post-reconstruction, and σ_α, the 1σ error bound (Fig. 9), show that the data are within the locus of measurements from this sub-sample of the mocks.

The distribution of errors on α show that for mocks 80 % have $\sigma_{\alpha,\,\rm pre}/\sigma_{\alpha,\,\rm post} > 1$ showing tightening of the peak on average following density field reconstruction. Our detection in the data of the BAO peak using our model, which marginalizes over broad-band shape, is at the $\sim 1.9\sigma$ level pre-reconstruction and $\sim 1.8\sigma$ post-reconstruction. In the sub-sample of the mocks pre-reconstruction 18% have a detection higher than this and post-reconstruction this increases to 52%. The mean detection level pre/post-reconstruction for the mocks is 1.5σ and 1.8σ, respectively. This increase in the number of high significance detections in the mocks shows the expected trend that on average, density field reconstruction enhances the detection significance. The lower left plot in Fig. 9 shows however that in 28% of cases in the mock sample reconstruction lowers the significance of detection. The reduction of significance seen in the data is therefore likely a case of the data being one of these 'unlucky' samples. An expected reason for this population of 'unlucky' realizations in comparison to overwhelming improvement in the BOSS survey (Alam et al. 2017) is that the number density for this study is lower in the contributing redshift range than BOSS. The weighted distribution of 6dFGS has a dominant contribution to the large-scale signal at $z \sim 0.1$, which corresponds to $n \sim 1.5 \times 10^{-4}$ (as can be seen from Fig. 4) whereas BOSS has a reasonably constant number density at $n \sim 4 \times 10^{-4}$. This factor of $\sim$3 lower in density leads to a less sampled density field during reconstruction and noise in the calculated displacements. When comparing the pre-reconstruction significance detection to Beutler et al. (2011) we find a lower value; this is due to a number of conservative alterations. These include (1) a change in the fitting model to include polynomial terms that marginalize over the shape giving more freedom, (2) a change of fitting range from $10\,{\rm h}^{-1}$ Mpc $< s < 200\,{\rm h}^{-1}$ Mpc to $30\,{\rm h}^{-1}$ Mpc $< s < 200\,{\rm h}^{-1}$ Mpc and (3) the new covariance matrix made from the COLA-based mocks rather than lognormal realizations (but which has slightly larger covariance amplitude).

6.3 Robustness tests

To investigate the robustness of the post-reconstruction BAO detection and the uncertainty on α, tests are run where parameters are systematically varied in both the fitting procedure and density field reconstruction.

During the post-reconstruction analysis, our default procedure uses 17 bins between $30\,{\rm h}^{-1}$ Mpc $< s < 200\,{\rm h}^{-1}$ Mpc and takes the non-linear damping as that from the mean of the mocks with a small prior. To test the robustness of the procedure, the scale over which the fitting occurs and also the damping scale are varied. The damping scale was fixed both at the value for the mean of the mocks and also held at $\Sigma_{\rm nl} = 0\,{\rm h}^{-1}$ Mpc (the value that given complete freedom this parameter tends towards). In testing the robustness against binning, the post-reconstruction analysis was conducted with correlation function binning $\Delta s = 8\,{\rm h}^{-1}$ Mpc, $12\,{\rm h}^{-1}$ Mpc, and $10\,{\rm h}^{-1}$ Mpc with the bins shifted to separations $5\,{\rm h}^{-1}$ Mpc larger in comparison to the standard pipeline.

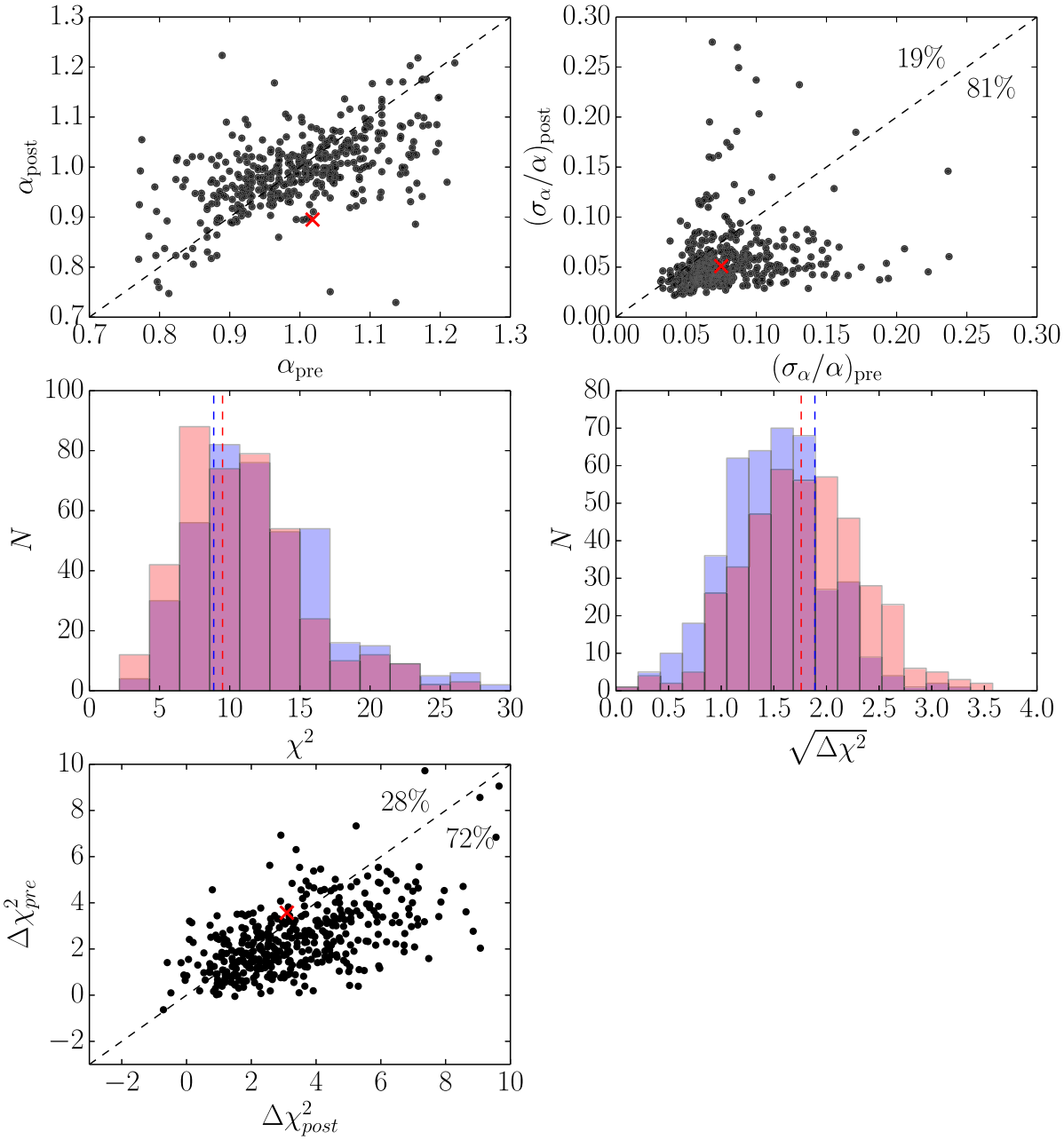

Figure 9. The distribution of (upper left) α, (upper right) σ_α, (middle left) χ^2, (middle right) $\sqrt{\Delta\chi^2}$ (significance of detection), (lower left) $\Delta\chi^2$ comparison pre/post-reconstruction for the mock sample that have been cut for outliers and to realizations that have 1σ contours fully within the prior range ($0.7 < \alpha < 1.3$). The data (red crosses in scatter plots and dashed lines blue for pre-reconstruction/red for post-reconstruction in the histograms) are within the range of the mock catalogues that show improvement following density field reconstruction. The lower left plot shows how the $\Delta\chi^2$ between a BAO and no-BAO model increases in 72% of cases indicating an improvement in detection significance.

When testing the robustness of the post-reconstruction result the input survey linear bias is varied from $b = 1.82$ by ± 0.15 and also the smoothing kernel used on the density field is varied from $15\,h^{-1}$ Mpc by $\pm 5\,h^{-1}$ Mpc. Test results are collated in Table 1 and described below:

(i) Having a best fit $\alpha \sim 0.9$ is robust for all test cases. However, the uncertainty of α depends on the scales fitted. Changing the scales over which the fit was made in these three cases varied the uncertainty by $\Delta(\sigma_\alpha) = 0.01$.

(ii) Given complete freedom, the non-linear damping scale tends to $0\,h^{-1}$ Mpc, although only weakly preferred in comparison to the value found from the mean of the mocks, $\Delta\chi^2 = 0.08$. However, although it does not make a large difference in χ^2 it does impact σ_α by decreasing it at the $\Delta(\sigma_\alpha) = 0.01$ level. As the use of $\Sigma_{\rm nl} = 0\,h^{-1}$ Mpc would likely underestimate the uncertainty present, our default procedure is to place a small prior on the value centred on the mean recovered from the mocks. The value of α though remains robust against the chosen value of the smoothing scale.

Table 1. The results of a number of robustness tests applied to the 6dFGS post-reconstruction data. The first set of tests vary the scale over which our template is fit, the second set uses variations of the damping scale fixed at both the exact value located from the mean of the mocks and $0\,h^{-1}$ Mpc (which is the value preferred if left completely free). Thirdly, we vary the binning used in the correlation function when fitting against the model from $10\,h^{-1}$ Mpc to $8\,h^{-1}$ Mpc, $12\,h^{-1}$ Mpc and also displacing the bin centres by $5\,h^{-1}$ Mpc. During reconstruction parameter tests we vary the linear galaxy bias b input ± 0.15 and finally the scale of smoothing R in the Gaussian kernel by $\pm 5\,h^{-1}$ Mpc.

Test	α	χ^2/d.o.f
Normal pipeline	0.895 ± 0.042	9.49/11
Fitting procedure		
(i)		
$20\,h^{-1}$ Mpc $< s <$ $200\,h^{-1}$ Mpc	0.902 ± 0.041	10.78/12
$40\,h^{-1}$ Mpc $< s <$ $190\,h^{-1}$ Mpc	0.895 ± 0.032	8.33/9
$50\,h^{-1}$ Mpc $< s <$ $180\,h^{-1}$ Mpc	0.895 ± 0.035	8.20/7
(ii)		
$\Sigma_{\rm nl} = 4.5\,h^{-1}$ Mpc fixed	0.902 ± 0.041	9.50/12
$\Sigma_{\rm nl} = 0\,h^{-1}$ Mpc	0.887 ± 0.031	9.42/12
(iii)		
$\Delta s = 8\,h^{-1}$ Mpc	0.913 ± 0.112	11.93/15
$\Delta s = 12\,h^{-1}$ Mpc	0.929 ± 0.036	5.91/7
$\Delta s = 10\,h^{-1}$ Mpc ($+5\,h^{-1}$ Mpc)	0.96 ± 0.067	9.44/11
Reconstruction parameters		
(iv)		
$b = 1.67$	0.898 ± 0.098	12.34/11
$b = 1.97$	0.890 ± 0.047	9.79/11
$R = 10\,h^{-1}$ Mpc	0.911 ± 0.043	9.54/11
$R = 20\,h^{-1}$ Mpc	0.897 ± 0.046	10.15/11
$f = 0.537$	0.895 ± 0.036	11.17/11
$f = 0.637$	0.889 ± 0.046	10.72/11

Table 2. Summary table of results from the analysis.

Result	$D_V\,(r_s^{\rm fid}/r_s)$ (Mpc)	χ^2/ν
6dF only – Pre-recon	$423 \pm 27(\pm^{74}_{48})$ ($z_{\rm eff} = 0.097$)	0.81
6dF only – Post-recon	$372 \pm 17(\pm^{98}_{33})$ ($z_{\rm eff} = 0.097$)	0.86
Joint Result – Post-recon	$539 \pm 17(\pm^{35}_{39})$ ($z_{\rm eff} = 0.122$)	1.14
Cosmological parameters	(combined with Planck prior)	
Ω_m	0.346 ± 0.045	
H_0	64.0 ± 3.5 km s^{-1} Mpc	

(iii) We have also tested changing the binning of the correlation function and covariance matrix from our default of $10\,h^{-1}$ Mpc to $8\,h^{-1}$ Mpc, $12\,h^{-1}$ Mpc and also displacing the bin centres by $5\,h^{-1}$ Mpc whilst retaining the default width. In all cases the value of α post-reconstruction varies within the 1σ error and σ_α is within $\Delta(\sigma_\alpha) = 0.01$, except for the $8\,h^{-1}$ Mpc. In this case the likelihood has given weighting to the sub-dominant peak widening the overall distribution at the 1σ level.

(iv) When varying the linear bias used during density field reconstruction by ± 0.15 and also changing the smoothing kernel scale, α is found to only change by 1.5%. The robustness against smoothing kernel scale is similar to that seen in Burden et al. (2014) when varing R for CMASS and LOWZ.

Varying f during the reconstruction only tested the robustness against a sub-optimal RSD removal. In these cases we found that a variation of f by ∼8% resulted in α varying by $< 1\%$.

Comparing how these changes in reconstruction parameters translate through to BAO detection significance we find little change. Our standard pipeline gives 1.8σ then $b = 1.67$ gives 1.6σ, $b = 1.97$ gives 1.7σ, $R = 10\,h^{-1}$ Mpc gives 1.6σ, $R = 20\,h^{-1}$ Mpc gives 1.6σ, $f = 0.537$ gives 1.8σ and $f = 0.637$ gives 1.7σ. These significances of detection reflect the noise level inherent in the 6dFGS likelihood.

7 COSMOLOGICAL INTERPRETATION

In this section, we convert our measurement of α to a volume-averaged distance and combine with the $\Omega_m h^2$ and $\Omega_b h^2$ priors from Planck 2015 to constrain H_0 and the cosmological parameters. Combining the joint clustering measurement with $\Omega_m h^2$ from the CMB calibrates the standard ruler.

7.1 6dFGS post-reconstruction only

The best-fitting constraint post-reconstruction translates to $D_V(z_{\rm eff} = 0.097) = \alpha D_V^{\rm fid}(z_{\rm eff} = 0.097)(r_s/r_s^{\rm fid}) = \left[372 \pm 17(\pm^{98}_{33})\right]\,(r_s/r_s^{\rm fid})$ Mpc with $D_V^{\rm fid}(z_{\rm eff} = 0.097) = 416$ Mpc. This result is consistent with our fiducial cosmology at the 2σ level. Although the measured value of α is reasonably far from 1, the likelihood shows a strong bimodal shape (see Fig. 7).

7.2 Combined analysis with SDSS DR7 MGS

The SDSS DR7 MGS was analysed using density field reconstruction in Ross et al. (2015), finding a 4 % distance measurement at $z_{\rm eff} = 0.15$. By combining the likelihoods from SDSS MGS and 6dFGS post-reconstruction we consider the relative contributions of both surveys. The SDSS MGS is a predominately Northern hemisphere survey and 6dFGS is a mainly Southern hemisphere survey. This large angular separation between surveys means there exists only a 3% overlap between SDSS MGS and 6dFGS and the redshift distribution is sufficiently different, such that the covariance between surveys has a negligible contribution to the result.

A joint constraint between the post-reconstruction 6dFGS and SDSS MGS is obtained by multiplicatively combining the likelihoods, taking the consensus $\xi(s) + P(k)$ result for SDSS MGS available as a supplement from Ross et al. (2015), which alone gives $\alpha = 1.040 \pm 0.037$. When these likelihoods are combined a constraint of $\alpha = 1.040 \pm 0.032$ is obtained. The individual $\Delta\chi^2$ distributions are shown in Fig. 10. Although the majority of the information comes from SDSS MGS, 6dFGS adds enough information to provide an improvement of ∼14% on the SDSS MGS result.

Taking this joint constraint on α we can provide a distance measurement at the effective volume weighted redshift of joint 6dFGS and SDSS MGS, $z_{\rm eff}^{\rm joint} = 0.122$, of $D_V(z_{\rm eff} = 0.122) = \left[539 \pm 17(\pm^{35}_{39})\right]\,(r_s/r_s^{\rm fid})$ Mpc, with $D_V^{\rm fid}(z_{\rm eff} = 0.122) = 519$ Mpc. The joint post-reconstruction measurement of the distance is compared with the other survey results in Fig. 11, and also to the fiducial flat ΛCDM cosmology in the redshift range $z < 0.8$.

7.3 Combining with the Planck 2015 $\Omega_m h^2$ prior

The ratio of D_V/r_s can be constructed by using a numerically calibrated analytical approximation (Aubourg et al. 2015) to CAMB of

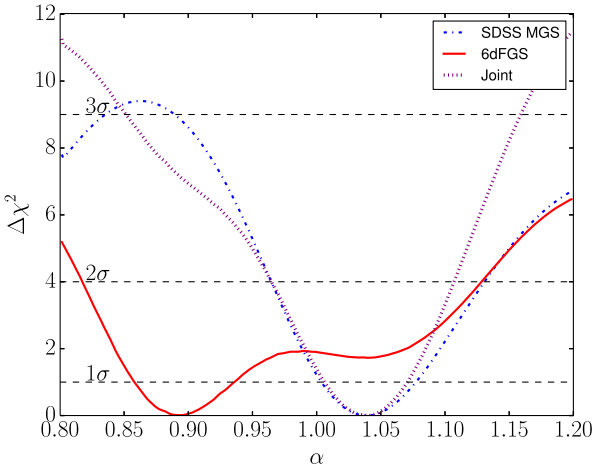

Figure 10. The $\Delta\chi^2$ distributions of α post-reconstruction 6dFGS (red), SDSS MGS (green), and joint (purple). The dashed lines show the 1σ, 2σ, and 3σ contours. The enhancement of a joint constraint over SDSS MGS alone is apparent at the 1σ level and increasingly so at higher confidence intervals.

the sound horizon at the drag epoch (fiducial $r_s^{\rm fid}(z_d) = 147.5\,{\rm Mpc}$)

$$r_s = 55.154 \frac{\exp(-72.3(\Omega_\nu h^2 + 6\times10^{-4})^2)}{(\Omega_b h^2)^{0.12807}(\Omega_m h^2 - \Omega_\nu h^2)^{0.2535}}, \quad (19)$$

which can be propagated through to give a degeneracy contour in the H_0–Ω_m parameter space. In the above analytical expression Ω_ν and Ω_b are the density parameters for neutrinos and baryons with values 1.4×10^{-3} and 0.0484 (Planck Collaboration et al. 2015; Haridasu, Lukovic & Vittorio 2018), respectively. Taking the $\Omega_m h^2$ prior from the Planck 2015 results ($\Omega_m h^2 = 0.1417 \pm 0.024$; Planck Collaboration et al. 2015) the degeneracy can be broken

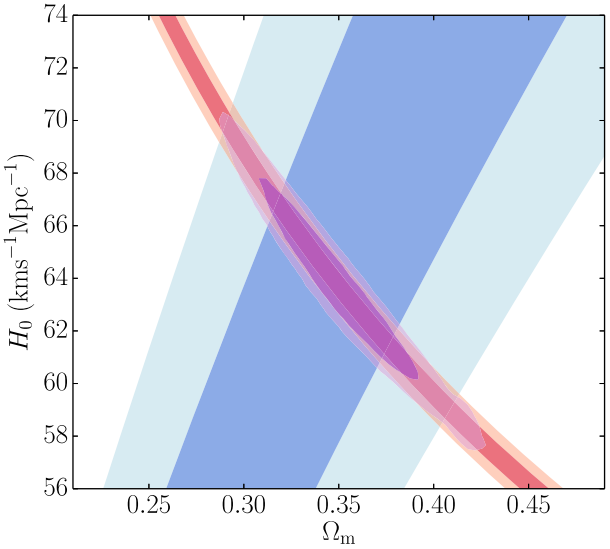

Figure 12. H_0–Ω_m parameter contours from the Planck 2015 $\Omega_m h^2 = 0.1417 \pm 0.024$ prior (red) and the $D_v/r_s = 3.66 \pm 0.12$ (blue) measurements from the combined constraint of 6dFGS and SDSS MGS. Combining these individual constraints breaks the degeneracy to give a combined contour (purple) that allows for a measure of H_0 and Ω_m. The corresponding results are given in Section 7.3 and Table 2.

to provide a measurement of $H_0 = 64.0 \pm 3.5\,{\rm km\,s^{-1}}$ Mpc and $\Omega_m = 0.346 \pm 0.045$. A plot showing the joint fit H_0–Ω_m contour with the Planck $\Omega_m h^2$ prior is given in Fig. 12. This measurement of the Hubble parameter is consistent with other BAO and CMB experiments. However, they are in tension with current supernova distance ladder measurements (Riess et al. 2016) at $\sim 2.4\sigma$.

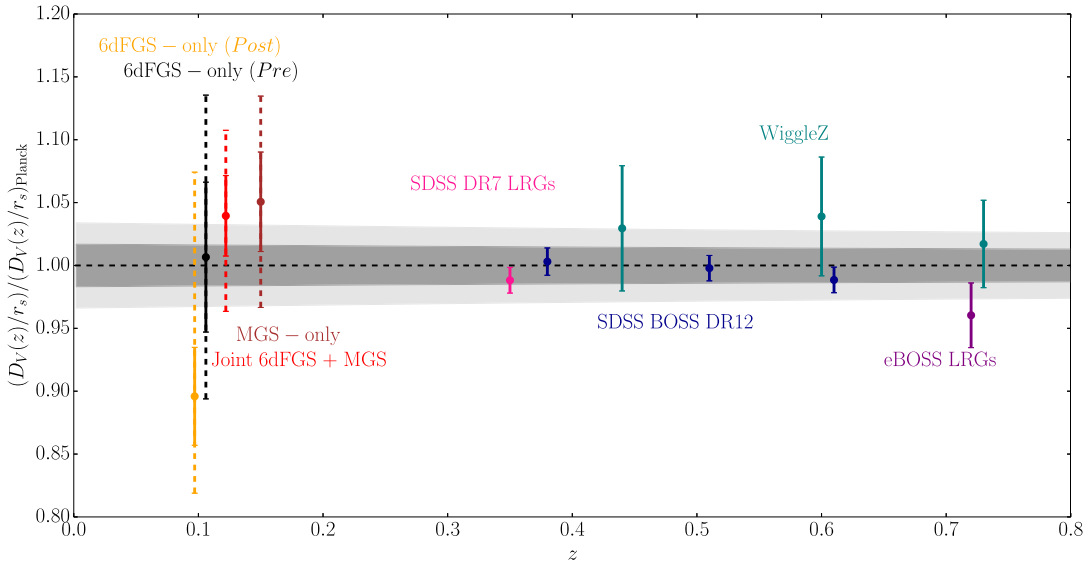

Figure 11. Distance constraints of low-redshift measurements SDSS DR7 LRGs (Padmanabhan et al. 2012), BOSS DR12 (Alam et al. 2017), eBOSS LRGs (Bautista et al. 2017), WiggleZ (Kazin et al. 2014), and the joint 6dFGS/SDSS MGS (Beutler et al. 2011; Ross et al. 2015) constraint of $\alpha = 1.040 \pm 0.032$. For comparison purposes we focus on measurements at $z < 0.8$; higher redshift measurements exist for both eBOSS QSO and BOSS Lyα. The dashed line corresponds to a flat ΛCDM model matching the Planck 2015 best fit, with the 1σ and 2σ confidence intervals being the shaded dark and light grey regions, respectively. The pre-reconstruction 6dFGS result is from Beutler et al. (2011) and the post-reconstruction is from this work. Error-bars are solid for 1σ and dashed for 2σ (focussing on the datasets used); it should be remembered that the post-reconstruction result from 6dFGS alone has a non-Gaussian likelihood such that the ΛCDM cosmology is consistent at the 2σ level.

8 CONCLUSION

We have updated the BAO analysis of 6dFGS presented in Beutler et al. (2011). Changes made to the analysis pipeline in comparison to that work include:

(i) Production of 600 COLA based fast mock catalogues over periodic boxes of size $1.2\,h^{-1}$ Gpc, populated with galaxies to describe the 6dFGS data through the application of a HOD modelling on top of a FoF halo finder. These mocks offer a more accurate covariance matrix with which to perform the analysis in comparison to the lognormal realizations generated in previous work.

(ii) An FFT version of density field reconstruction has been applied to the 6dFGS data and mock realizations.

(iii) We make use of a correlation function model that is now commonly used in SDSS (MGS and BOSS) BAO analyses. This model, unlike the previous work, allows for freedom in the broad-band shape by introducing polynomial terms over which to marginalize. This marginalization is imperative when dealing with the post-reconstruction two-point statistics, as a well-defined physical model for the broad-band shape is still not known. This procedure also ensures that the information being used in the constraint is coming solely from the peak position.

Overall we find that, in the sub-sample of the mock catalogues that show a detection of the BAO peak both pre/post-reconstruction, 81% show an improvement after the application of density field reconstruction to remove non-linear shifts of the galaxy positions, and the significance of detection improves on average. In the mean of the mock population an improvement factor of $I = \sigma_{\alpha,\,\mathrm{pre}}/\sigma_{\alpha,\,\mathrm{post}} \sim 1.86$ is seen. In the data catalogue, pre-reconstruction we find consistency with the previous analysis of Beutler et al. (2011). In performing density field reconstruction on the data introduces bi-modality into the likelihood that we argue is likely a statistical fluctuation relative to the mock catalogues. At the 1σ confidence interval the error drops from ∼6.6% to ∼4.1%, however due to the non-Gaussian nature of the post-reconstruction likelihood the significance of detection drops from $\sim 1.9\sigma$ to $\sim 1.8\sigma$. This decrease in statistical significance post-reconstruction is displayed in 28% of the mock sample suggesting it is consistent with statistical fluctuations within the population. The measurements agree with the flat ΛCDM Planck based cosmology at the 2σ level.

By combining the post-reconstruction result with that from SDSS MGS at $z_{\mathrm{eff}} = 0.15$, we obtain a joint constraint of $\alpha(z_{\mathrm{eff}} = 0.122) = 1.040 \pm 0.032$. The likelihood of 6dFGS offers an ∼14% improvement on the SDSS MGS result at the 1σ level. At higher confidence intervals this improvement is even greater showing that we are pinning down the tails of the likelihood distribution. Using the $\Omega_m h^2$ prior from Planck 2015 results, the degeneracy of the joint 6dFGS and SDSS MGS D_V/r_s constraint in the Ω_m–H_0 plane is broken, as shown in Fig. 12. This provides cosmological parameter constraints of $H_0 = 64.0 \pm 3.5\,\mathrm{km\,s^{-1}}$ Mpc and $\Omega_m = 0.346 \pm 0.045$. The final measurements of D_V are collated in Table 2. While these results are consistent with the currently accepted Planck ΛCDM model, they are in 2.4σ tension with the latest Supernova Ia results ($H_0 = 73.24 \pm 1.74\,\mathrm{km\,s^{-1}}$ Mpc; Riess et al. 2016).

This work constitutes the current best constraint available from BAO in the low-redshift ($z < 0.3$) regime. In the near future both the Taipan Galaxy Survey (da Cunha et al. 2017) and DESI (DESI Collaboration et al. 2016) will target this low-redshift regime providing measurement of BAO at the 1% level. These will further study any potential late-time deviations from the currently accepted ΛCDM model.

ACKNOWLEDGEMENTS

PC and WJP acknowledge support from the European Research Council through the Darksurvey grant 614030. WJP also acknowledges support from the UK Science and Technology Facilities Council grant ST/N000668/1 and the UK Space Agency grant ST/N00180X/1. FB is a Royal Society University Research Fellow. JK is supported by MUIR PRIN 2015 'Cosmology and Fundamental Physics: Illuminating the Dark Universe with Euclid' and Agenzia Spaziale Italiana agreement ASI/INAF/I/023/12/0. Parts of this research were conducted by the Australian Research Council Centre of Excellence for All-sky Astrophysics (CAASTRO), through project number CE110001020. The 6dF Galaxy Survey had many contributions to the instrument, survey and science, in particular we thank Matthew Colless, Heath Jones, Will Saunders, Fred Watson, Quentin Parker, Mike Read, Lachlan Campbell, Chris Springob, Christina Magoulas, John Lucey, Jeremy Mould, and Tom Jarrett, as well as the staff of the Australian Astronomical Observatory and other members of the 6dFGS team. This project has made use of the SCIAMA High Performance Computing (HPC) cluster at the ICG and also the GREEN-II Supercomputer in Swinburne. This work was supported by the Flagship Allocation Scheme of the NCI National Facility at the ANU.

REFERENCES

Achitouv I., Blake C., Carter P., Koda J., Beutler F., 2017, Phys. Rev., 95, 083502
Alam S. et al., 2017, MNRAS, 470, 2617
Anderson L. et al., 2014, MNRAS, 441, 24
Ata M. et al., 2018, MNRAS, 473, 4773
Aubourg E. et al., 2015, Phys. Rev., 92, 123516
Bautista J. E. et al., 2017, ApJ, 863, 110
Beutler F. et al., 2011, MNRAS, 416, 3017
Beutler F. et al., 2013, MNRAS, 429, 3604
Bianchi D., Percival W. J., 2017, MNRAS, 472, 1106
Blake C. et al., 2011, MNRAS, 415, 2892
Blake C., Carter P., Koda J., 2018, MNRAS, 479, 5168
Bullock J. S., Kolatt T. S., Sigad Y., Somerville R. S., Kravtsov A. V., Klypin A. A., Primack J. R., Dekel A., 2001, MNRAS, 321, 559
Burden A., Percival W. J., Manera M., Cuesta A. J., Vargas Magana M., Ho S., 2014, MNRAS, 445, 3152
Burden A., Percival W. J., Howlett C., 2015, MNRAS, 453, 456
Cole S. et al., 2005, MNRAS, 362, 505
Colless M. et al., 2001, MNRAS, 328, 1039
Cooray A., Sheth R., 2002, Phys. Rep., 372, 1
Crocce M., Scoccimarro R., 2008, Phys. Rev., 77, 023533
da Cunha E. et al., 2017, PASA, 34, e047
de la Torre S. et al., 2013, A&A, 557, A54
Delubac T. et al., 2015, A&A, 574, A59
DESI Collaboration et al., 2016, preprint (arXiv:1611.00036)
Di Valentino E., Melchiorri A., Silk J., 2016, Phys. Lett., 761, 242
Eisenstein D. J., Hu W., 1998, ApJ, 496, 605
Eisenstein D. J. et al., 2005, ApJ, 633, 560
Eisenstein D. J., Seo H.-J., White M., 2007a, ApJ, 664, 660
Eisenstein D. J., Seo H.-J., Sirko E., Spergel D. N., 2007b, ApJ, 664, 675
Feldman H. A., Kaiser N., Peacock J. A., 1994, ApJ, 426, 23
Font-Ribera A. et al., 2014, JCAP, 5, 027
Guo H. et al., 2015, MNRAS, 446, 578
Guo H. et al., 2016, MNRAS, 459, 3040
Hamilton A. J. S., 1998, in Hamilton D., ed., Astrophysics and Space Science Library. Vol. 231, The Evolving Universe, p. 185
Haridasu B. S., Luković V. V., Vittorio N., 2018, JCAP, 5, 033
Hartlap J., Simon P., Schneider P., 2007, A&A, 464, 399
Hawkins E. et al., 2003, MNRAS, 346, 78
Howlett C., Manera M., Percival W. J., 2015, Astron. Comput., 12, 109

Jones D. H. et al., 2004, MNRAS, 355, 747
Jones D. H., Peterson B. A., Colless M., Saunders W., 2006, MNRAS, 369, 25
Jones D. H. et al., 2009, MNRAS, 399, 683
Kaiser N., 1987, MNRAS, 227, 1
Kazin E. A. et al., 2010, ApJ, 710, 1444
Kazin E. A. et al., 2014, MNRAS, 441, 3524
Kitaura F.-S. et al., 2016, Phys. Rev. Lett., 116, 171301
Koda J., Blake C., Beutler F., Kazin E., Marin F., 2016, MNRAS, 459, 2118
Landy S. D., Szalay A. S., 1993, ApJ, 412, 64
Lewis A., Challinor A., Lasenby A., 2000, ApJ, 538, 473
Liang Y., Zhao C., Chuang C.-H., Kitaura F.-S., Tao C., 2016, MNRAS, 459, 4020
Ma C.-P., Fry J. N., 2000, ApJ, 531, L87
Navarro J. F., Frenk C. S., White S. D. M., 1996, ApJ, 462, 563
Noh Y., White M., Padmanabhan N., 2009, Phys. Rev., 80, 123501
Padmanabhan N., White M., Cohn J. D., 2009, Phys. Rev., 79, 063523
Padmanabhan N., Xu X., Eisenstein D. J., Scalzo R., Cuesta A. J., Mehta K. T., Kazin E., 2012, MNRAS, 427, 2132
Peacock J. A., Smith R. E., 2000, MNRAS, 318, 1144
Pearson D. W., Samushia L., 2017, MNRAS, 478, 4500
Percival W. J. et al., 2001, MNRAS, 327, 1297
Percival W. J. et al., 2010, MNRAS, 401, 2148
Planck Collaboration et al., 2015, A&A, 594, A13
Riess A. G. et al., 2016, ApJ, 826, 56
Ross A. J., Samushia L., Howlett C., Percival W. J., Burden A., Manera M., 2015, MNRAS, 449, 835
Schmittfull M., Feng Y., Beutler F., Sherwin B., Chu M. Y., 2015, Phys. Rev., 92, 123522
Seljak U., 2000, MNRAS, 318, 203
Seo H.-J., Eisenstein D. J., 2007, ApJ, 665, 14
Slepian Z. et al., 2017, MNRAS, 469, 1738
Slosar A. et al., 2013, JCAP, 4, 026
Tassev S., Zaldarriaga M., Eisenstein D. J., 2013, JCAP, 6, 036
van den Bosch F. C., Norberg P., Mo H. J., Yang X., 2004, MNRAS, 352, 1302
Weinberg D. H., Mortonson M. J., Eisenstein D. J., Hirata C., Riess A. G., Rozo E., 2013, Phys. Rep., 530, 87
York D. G. et al., 2000, AJ, 120, 1579
Zehavi I. et al., 2011, ApJ, 736, 59
Zel'dovich Y. B., 1970, A&A, 5, 84
Zheng Z. et al., 2005, ApJ, 633, 791

This paper has been typeset from a TEX/LATEX file prepared by the author.